Research article

Preclinical characterization of Pan-NKG2D ligand-binding NKG2D receptor decoys

Peter B. Rupert [a], Matthew Buerger [a], Emily J. Girard [b,1], Marie Frutoso [a,1],
Don Parrilla [a,1], Kevin Ng [a], Theodore Gooley [a], Veronika Groh [a], Roland K. Strong [a,*]

[a] *Division of Basic Science, Fred Hutchinson Cancer Center, Seattle, WA, United States*
[b] *Clinical Research Division, Fred Hutchinson Cancer Center, Seattle, WA, United States*

ABSTRACT

NKG2D and its ligands are critical regulators of protective immune responses controlling infections and cancer, defining a crucial immune signaling axis. Current therapeutic efforts targeting this axis almost exclusively aim at enhancing NKG2D-mediated effector functions. However, this axis can drive disease processes when dysregulated, in particular, driving stem-like cancer cell reprogramming and tumorigenesis through receptor/ligand self-stimulation on tumor cells. Despite complexities with its structure and biology, we developed multiple novel engineered proteins that functionally serve as axis-blocking NKG2D "decoys" and report biochemical, structural, *in vitro*, and *in vivo* evaluation of their functionality.

1. Introduction

The stimulatory natural killer group 2 lymphocyte receptor D (NKG2D) and its induced-self ligands (NKG2D-L) constitute a critical immune response against cellular distress, infection, and malignancy. Signaling through the NKG2D/NKG2D-L axis enables detection of viral infection or oncogenic transformation, with the presence of NKG2D-L associated with rejection of nascent tumors and viral clearance [1]. NKG2D is a type II, transmembrane-anchored, C-type lectin-like receptor expressed on the surface of all natural killer (NK) cells, CD8 T cells, invariant NKT cells, γδ T cells, and subpopulations of CD4 T cells and innate lymphoid cells [2–4]. Upon ligand engagement, NKG2D elicits cytotoxic, pro-inflammatory cytokine, and/or chemokine responses, either directly or via co-stimulation [2,5]. In humans, NKG2D forms disulfide-linked homodimers that gain stable surface expression and functionality through assembly with four chains of the signaling adaptor protein DNAX-activating protein 10 (DAP10) [6,7]. Ligation of NKG2D results in phosphorylation of DAP10 at a tyrosine-based activation motif (ITAM) followed by recruitment of either phosphoinositide 3-kinase (PI3K) or the growth factor receptor-bound protein 2 (Grb2)/Vav1, which in turn activate protein kinase B (PKB/AKT) and mitogen-activated protein kinase (MAPK) signaling cascades and their downstream effector functions [6,8].

NKG2D-L are structurally homologous to major histocompatibility complex class I (MHC-I) proteins but lack antigen presentation functions. In humans, NKG2D-L include MHC-I polypeptide-related sequence A (MICA) and B (MICB) proteins, and the human cytomegalovirus glycoprotein UL16-binding protein family (ULBP1-6) [9]. NKG2D-L are largely absent from the surface of normal

---

cells, but they can be induced by multiple mechanisms associated with cellular stress, viral transactivation, or oncogenic transformation [10,11].

Although evolved for protective roles in immune responses to unhealthy cells, NKG2D and its ligands can become drivers of disease processes when dysregulated. This is particularly apparent in several autoinflammatory conditions, progressing tumors, and organ transplantation [12–16]. For example, inflammation-induced expression of NKG2D-L on intestinal epithelial cells or synovial fibroblasts paired with cytokine-activated NKG2D on tissue-resident CD8 or pro-inflammatory CD4 T cells has been implicated in the pathogenesis of celiac disease, inflammatory bowel disease, and in rheumatoid arthritis [3,5,17]. Similarly, aberrant expression of NKG2D-L in hair follicles in concert with heightened NKG2D functionality in skin CD8 T cells cause hair loss in alopecia areata [18]. In support of a crucial role of the NKG2D pathway in autoinflammation, a recent clinical trial administering an anti-NKG2D antibody to patients with Crohn's disease showed some clinical efficacy [19]. The NKG2D/NKG2D-L axis also contributes to graft rejection in solid organ transplants: MICA and MICB expression in transplanted kidneys and pancreas is associated with cellular injury, and the presence of anti-MICA autoantibodies positively correlates with graft rejection [16]. NKG2D signaling also contributes to undesired outcomes in the manufacture of NKG2D chimeric antigen receptor (CAR) T or NK cells through activation-induced NKG2D-L expression on T cells or NK cells, leading to fratricide [20].

In the perhaps most unexpected deviation from its canonical function, NKG2D can moonlight as a driver of stem-like cancer cell reprogramming and tumorigenesis. We recently discovered that subsets of cancer cells in breast, ovarian, colon, and prostate cancer express signaling-competent NKG2D receptors to exploit the presence of tumor-associated NKG2D-L for self-stimulation of tumor initiation and progression [13,14]. In ovarian cancer, this NKG2D-driven tumorigenesis underlies the disease progression associated with expression of NKG2D-L [14].

Current therapeutic efforts targeting the NKG2D/NKG2D-L axis almost exclusively aim at enhancing protective NKG2D-mediated effector functions [21]. Such approaches may be counterproductive in NKG2D-driven autoimmune conditions and in progressing tumors with NKG2D expressing cancer cells. Anti-NKG2D antibody-based inhibition has been attempted but carries with it the risk of unintended receptor activation via antibody-mediated NKG2D crosslinking [17]. Blocking the NKG2D/NKG2D-L axis using anti-NKG2D-L antibodies is complicated, as NKG2D-L expression on any given cell almost always involves more than one ligand type and is heterogeneous in both inflamed and cancerous tissues [1]. To accommodate this heterogeneity, and the possibility of undesired antibody-crosslinking effects, we developed a soluble NKG2D receptor "*decoy*" reagent consisting of seven NKG2D "*single chain dimers*" $(NKG2D_7^{SCD})$ [14]. $NKG2D_7^{SCD}$ bound to all known NKG2D-L and, in a preliminary *in vivo* study, antagonized oncogenic tumor cell NKG2D signaling in patient-derived ovarian cancer xenotransplants [14]. This outcome prompted formal preclinical testing of $NKG2D_7^{SCD}$ and of two additional $NKG2D^{SCD}$-based constructs, including a bivalent, antibody Fc-dimerized reagent $(NKG2D_2^{SCD})$ and a monovalent, single-SCD reagent $(NKG2D_1^{SCD})$. Here we report structural analyses of the ~100-fold increase in affinity of SCD *vs.* native NKG2D [14], using "*pre-stabilized*" variants of MICA for co-crystallization, and compare *in vitro* and *in vivo* functionality, including pharmacokinetics, pharmacodynamics and *in vivo* NKG2D blocking efficiency, of the $NKG2D^{SCD}$ compounds with the goal to determine the optimal choice for further clinical development.

2. Materials and methods

Cell Lines and Transfectants. HEK293T (American Type Culture Collection (ATCC) CRL-3216), HEK293FT (Thermo Fisher #R70007; RRID: CVCL_6911), FreeStyle 293-F cells (Thermo Fisher #R79007; RRID: CVCL_D6642), and MDAH-2774 (ATCC CRL-10303; RRID: CVCL_0420) cells were grown in Dulbecco's modified Eagle medium (DMEM; ATCC #30–2002) plus 10% fetal bovine serum (FBS; Thermo Fisher #C838T70) or FreeStyle 293 medium (Thermo Fisher #12338001). Cells were used within 25 passages within 3–4 months of revival. MDAH-2774–derived NKG2D-DAP10 transfectants (MDAH- 2774-TF) have been previously described [22] and were grown in in DMEM plus 10% FBS. C1R-MICA, C1R-MICB, C1R-ULBP1, C1R-ULBP2, EL4-ULBP3, Mel-ULBP4, EL4-ULBP5, and C1R-ULBP6 transfectants have been previously described [23] and were grown in RPMI-1640 (ATCC #30–2001) plus 10% FBS. Ectopic expression of NKG2D or NKG2D-L was confirmed by flow cytometry prior to experimental use as previously demonstrated [14].

Protein engineering, expression, and purification. MICA variants DSM20 and DSM25 were provided by AvidBiotics (San Francisco, CA); the previous heptameric construct $(NKG2D_7^{SCD})$ was produced and purified as previously described [14]. For crystallization, isolated human $NKG2D^{SCD}$ was produced with two modifications. First, the human C4b binding protein multimerization motif was deleted from $NKG2D_7^{SCD}$ to yield monomeric $NKG2D^{SCD}$ after proteolytic cleavage of the fusion partner with Tobacco Etch Virus protease (TEV) [24]. Second, $NKG2D^{SCD}$ was produced in FreeStyle 293-F cells treated with kifunensine [25], to reduce N-glycan heterogeneity [25]. Complexes of DSM20 and DSM25 with $NKG2D^{SCD}$ were obtained by mixing the proteins together, additionally treating with PNGase F (for $DSM20/NKG2D^{SCD}$) and isolating stoichiometric complexes by size-exclusion chromatography (SEC; GE Superdex 200 10/300 GL column). For functional studies, human $NKG2D_1^{SCD}$ and human and murine $NKG2D_2^{SCD}$ were assembled as N-terminal human Siderocalin (Scn)/Lipocalin 2 cleavable fusion proteins to improve yield [26]; $NKG2D_2^{SCD}$ was dimerized by incorporating human or murine IgG1 Fc domain sequences into the fusions. [Engineering and authentication of $NKG2D_7^{SCD}$ was previously described [14].] cDNAs encoding both fusion constructs were codon optimized for human cells (Genscript), synthesized (Genscript), and subcloned into optimized lentiviral vectors incorporating fluorescent reporter proteins [26]. [Native MICA, DSM20, DSM25, $NKG2D_1^{SCD}$, and $NKG2D_2^{SCD}$ protein sequences are provided as Supplementary Material.] Transductions and protein expression and purification were carried out as previously described [14,26]. Briefly, FreeStyle 293 cells were transduced, with near 100% efficiencies as judged by reporter fluorescence, at a density of 10^6 cells/mL in 10 mL Freestyle media. Cultures were grown to ~200 mL when comparative reduced/non-reduced SDS-PAGE was performed with 10x concentrated culture supernatant to determine

expression levels and confirm proper fusion protein folding. Cultures were expanded to 2 L and harvested at cell densities of ~3.5 × 10^6 cells/mL. Culture supernatants were filtered and supplemented with 150 mM NaCl before purification using HisTrap HP columns (Cytiva #17524701) on Cytiva ÄKTA pure FPLC systems. Columns were washed with phosphate-buffered saline (PBS) plus 10 mM imidazole and eluted with PBS plus 250 mM imidazole. The Scn-NKG2D$_2^{SCD}$ fusion protein was cleaved overnight at 4 °C with His-tagged TEV protease (produced in-house) at 3 mg/mL concentration at a 1:10 wt ratio in PBS plus 1 mM cysteine. TEV and uncleaved fusion were removed by re-running over HisTrap HP columns. NKG2D$_1^{SCD}$ and NKG2D$_2^{SCD}$ were further purified by SEC on a Superdex 200 column (GE Health Sciences) in PBS. Endotoxin levels were measured with an Endosafe Nexgen-PTS instrument (Charles River) using Endosafe LAL cartridges (Charles River) per the manufacturer's protocol. For flow cytometry, NKG2D^{SCD} fusion proteins were labeled with R-Phycoerythrin (PE; Sigma-Aldrich #52412) at a ratio of two fluorophores per molecule.

Crystallography. Diffraction-quality crystals of DSM25 were obtained from drops containing 14 mg/mL protein in 100 mM PIPES, 150 mM NaCl, 1 mM EDTA (pH = 7; PNE) by hanging-drop vapor diffusion over wells containing 110 mM D/L-Malic acid (pH = 7) and 20% w/w PEG3350 (Fisher Carbowax #P1463). Diffraction-quality crystals of the DSM25/NKG2D^{SCD} complex were obtained from drops containing 10 mg/mL protein in PNE by hanging-drop vapor diffusion over wells containing 100 mM HEPES (pH 7.2) and 35% w/w Jeffamine ED-2001 (Hampton Research #HR2-597). Diffraction-quality crystals of the DSM20/NKG2D^{SCD} complex were obtained from drops containing 11 mg/mL protein in PNE by hanging-drop vapor diffusion over wells containing 200 mM MgCl$_2$, 100 mM Tris (pH = 8.5), and 25% w/w PEG3350. Prior to data collection, crystals were transferred to their respective well solutions supplemented with 15–20% v/v glycerol and flash-cooled by plunging into liquid nitrogen. Diffraction data from DSM25 and DSM25/ NKG2D^{SCD} complex crystals were collected at the Advanced Light Source (ALS; Berkeley, CA) on beamline 5.0.1; diffraction data for the DSM20/NKG2D^{SCD} complex was collected on ALS beamline 5.0.2. All diffraction data were collected at a wavelength of 1.000 Å, and integrated and scaled with HKL-2000 [27]. Initial phases for the DSM25 structure ($z = 2$) were determined by molecular replacement using MOLREP [28] as implemented in the CCP4 software suite [29–31], using the coordinates of the α1α2 "*platform*" domain of MICA from 1HYR.pdb [32] as a search model. Initial phases for the DSM20/NKG2D^{SCD} ($z = 1$) and DSM25/NKG2D^{SCD} ($z = 1$) complexes were determined by molecular replacement with PHASER [33] using the coordinates of the NKG2D homodimer/MICA platform domain complex from 1HYR.pdb as a search model. Initial molecular replacement solutions were improved by rigid-body refinement with REFMAC [34], followed by iterative rounds of positional refinement using REFMAC and model building using COOT [35]. Crystallographic B-factors were modeled with a final round of TLS refinement [36]. Residues or side-chains that did not exhibit 2F$_{obs}$-F$_{calc}$ electron density when contoured at 0.7σ were removed or truncated at the Cβ atom. The quality of the final models was assessed by ProCheck [37] and Molprobity [38]. Ramachandran geometry values (calculated with ProCheck) are DSM25: 96.3% favored, 3.7% allowed; DSM25/NKG2D^{SCD}: 94.4% favored, 5.6% allowed, 0.1% outliers; and DSM20/NKG2D^{SCD}: 95.4% favored, 4.4% allowed. The final models have been deposited in the PDB [39] with accession codes 8TLZ (DSM25; overall Molprobity score: 0.8), 8TM2 (DSM25/NKG2D^{SCD}; overall Molprobity score: 1.73), and 8TM0 (DSM20/NKG2D^{SCD}; overall Molprobity score: 1.12). Complete crystallographic statistics are reported in Table 1.

Flow cytometry. Binding of NKG2D$_2^{SCD}$ to a panel of eight NKG2D-L transfected cell lines (C1R-MICA, C1R-MICB, C1R-ULBP1, C1R-ULBP2, EL4-ULBP3, Mel-ULBP4, EL4-ULBP5, and C1R-ULBP6 [23] was evaluated by flow cytometry to confirm specificity. 0.5 × 10^6 cells of each of the eight transfectant lines were treated with a cocktail of TruStain FcX Fc Receptor Blocking Solution (Biolegend #422301) plus LIVE/DEAD Fixable UV Blue Dead Cell Stain reagent (ThermoFisher #L23105) in PBS for 15 min at ambient in the

Table 1

Data collection and refinement statistics (molecular replacement).

	DSM25	DSM25 + NKG2D^{scd}	DSM20 + NKG2D^{scd}
PDB Accession Code	8TLZ	8TM0	8TM2
Data collection			
Space group	$P6_122$	$P2_12_12_1$	$P2_12_12_1$
Cell dimensions			
a, b, c (Å)	127.8, 127.8, 157.0	56.1, 68.4, 140.0	56.6, 69.8, 145.4
Resolution (Å)	50.00–2.75 (2.80–2.75)[a]	50.00–4.00 (4.07–4.00)[a]	50.00–2.85 (2.90–2.85)[a]
R_{merge}	5.5 (58.2)[a]	10.2 (54.2)[a]	7.4 (46.3)[a]
$I/\sigma I$	31.7 (5.8)[a]	10.3 (2.9)[a]	16.1 (2.2)[a]
Completeness (%)	99.9 (100.0)[a]	86.3 (88.2)[a]	83.2 (87.2)[a]
Redundancy	12.3 (12.2)[a]	2.8 (2.7)[a]	2.7 (2.7)[a]
Refinement			
Resolution (Å)	50.00–2.75	50.00–4.00	50.00–2.85
No. reflections	19,230/1054[b]	4290/233[b]	11,066/609[b]
R_{work}/R_{free}	23.1/27.0	26.9/36.2	21.4/25.2
No. atoms (average B-factor (Å^2))			
Protein	2643 (78)	3282 (120)	3332 (77)
Glycan	91 (112)	42 (156)	112 (80)
Other	74 (78)	–	28 [40]
R.m.s. deviations			
Bond lengths (Å)	0.01	0.01	0.01
Bond angles (°)	1.24	1.36	1.14

[a] Values in parentheses are for highest-resolution shell.
[b] Values are for all reflections/number of test reflections used for calculating R_{free}.

dark. Cells were washed with PBS plus 2% FBS, incubated with PE-conjugated $NKG2D_2^{SCD}$ for 20 min at ambient, and washed. Stained cell suspensions were fixed with BD Cytofix buffer (BD Biosciences #554655) for 20 min at ambient in the dark. Samples were analyzed using a FACSymphony A5 flow cytometer (BD Biosciences). Flow cytometry results were exported in FCS3.1 format and analyzed using FlowJo v10.6.x software (BD Life Sciences).

Immunohistochemistry. Immunohistochemistry was performed by the Fred Hutchinson Cancer Center (FHCC) Experimental Histopathology shared resource (RRID:SCR_0226120). 5-micron thick frozen sections of mouse tissue were air dried at ambient overnight, fixed in ice-cold acetone for 10 min, air dried for 1 h at room temperature, then again fixed in ice-cold acetone for another 10 min, and finally air dried for 1 h at ambient. Slides were stained on a BOND Rx autostainer (Leica) using Leica Bond reagents per the manufacturer's protocols. Endogenous peroxidase was blocked with 3% H_2O_2 for 5 min followed by protein blocking with 0.05 M Tris, 0.15 M NaCl, 0.25% w/w Casein, 0.1% v/v Tween 20, and 0.05% w/w Proclin 300 at pH 7.6 (TCT buffer) for 10 min. Prior to application the primary anti-ULBP-3 (mouse IgG_{2a}, R&D Systems; clone 166510; # MAB1517) mAb was complexed at a 1:2 ratio with AffiniPure Fab Fragment Rabbit Anti-Mouse IgG (H + L) (Jackson Labs #315-007-003) for 20 min, followed by a 10-min block of non-complexed secondary with normal mouse serum (Millipore Sigma #5905) at 20 μl/1 μg secondary. The complexed primary was applied at 0.5 μg/ml for 60 min and slides were then stained with anti-mouse HRP polymer (Leica #PV6114) for 12 min followed by Mixed Refine DAB (Leica #DS9800) for 10 min and counterstained with Refine Hematoxylin (Leica #DS9800) for 4 min. Slides were then dehydrated, cleared, and cover slipped with permanent mounting media. For analysis, slides were scanned on an ScanScope AT Turbo (Aperio) and on a TissueFAXS (TissueGnostics) instrument. Image analysis was performed by the FHCC Cellular Imaging shared resource (RRID:SCR_022609).

Animal Studies. All vertebrate animal experiments were approved under FHCC Animal Care and Use Committee protocols 50808 and 51040.

Biodistribution and pharmacokinetic studies. Proteins were exhaustively methylated using the procedures of [41,42] as previously described [43,44]. Briefly, protein was reacted with ^{14}C-formaldehyde (57 μCi/nmol; Pharmaron) and sodium cyanoborohydride at room temperature overnight, then purified using a Strata-X reversed-phase cartridge (Phenomenex). Serum pharmacokinetics were evaluated in six-to eight-week-old Balb/c mice (Envigo Labs #047) administered 10 nmol of ^{14}C-labeled protein as a 100 μl bolus by tail vein injection. Treatment groups consisted of 1) human $NKG2D_1^{SCD}$ (29.9 μCi/bolus), 2) murine/murine $NKG2D_2^{SCD}$ (29.56 μCi/bolus), 3) human/human $NKG2D_2^{SCD}$ (30.76 μCi/bolus), and 4) human $NKG2D_7^{SCD}$ (14.06 μCi/bolus). Three mice were randomly assigned to each treatment group. At intervals of 0.5, 1, 2, 4, 6, and 24 h after ^{14}C-protein administration, ~20ul of blood was collected from the saphenous vein for analysis by liquid scintillation counting. 2 μl (0.5–6 h time points) or 10 μl (24 h time point) of fresh whole blood was placed in 5 ml of Ultima-Gold liquid scintillant (PerkinElmer #6013321), vortexed, and counted on a Packard Tri-carb scintillation counter (PerkinElmer). The nmol/μl of protein in blood for each mouse at each time point was calculated from the recorded counts per minute using a pre-established dose titration slope under identical read conditions, volume of each sample analyzed, and the specific activity of each labeled protein. T_{max} (hours), C_{max} (nmol/μl), AUC (hours*nmol/μl), and $T_{1/2}$ were determined using PKSolver [45]. Quantitative whole-body autoradiography was performed and analyzed as previously described [43]. Briefly, 10 nmol of the ^{14}C-labeled proteins used for pharmacokinetic studies were each administered to two 6-week-old female athymic nude mice (Envigo #6902) xenografted with MDAH-2774-TF flank tumors and allowed to circulate. Mice were humanely euthanized 3 h after protein administration and nmol/g of tissue determined.

Anti-tumor efficacy studies. 6- to 8-week-old female and male nonobese diabetic/severe combined immunodeficient gamma (NOD SCID-$Il2rg^{-/-}$; NSG) mice were bred at the FHCC Core Center of Excellence in Hematology (CCEH) and housed under pathogen-free conditions at the FHCC Comparative Medicine shared resource. For implants, mice (5 females and 5 males per group) were injected subcutaneously into dorsal flanks with 1×10^3 viable MDAH-2774–TF cells in 100 μl growth medium (1:1 PBS/BD Matrigel Matrix; BD Bioscience # 356237) per [14]. Mice were treated at the time of implant and three times thereafter in weekly intervals with $NKG2D_2^{SCD}$, $NKG2D_1^{SCD}$, or PBS for *in vivo* NKG2D-L masking control administered via intravenous (tail vein) injection. Both $NKG2D^{SCD}$ reagents were administered in three dosages, each at either 500 μg, 250 μg or 50 μg per tail vein injection. Tumor development and growth was monitored by manual palpation and external vernier caliper (VWR). Tumor volume was calculated as $V = 4/3 \times \pi \times (L/2 \times W/2 \times W/2)$, with L = length and W = width. At experimental endpoints or when a tumor parameter reached 1.5 cm, whichever came first, animals were euthanized by carbon dioxide overdose. Tumors were resected, embedded in Tissue-Tek OCT Compound (Sakura #4583) on a dry ice and 2-methylbutane slurry, and stored at −80 °C. All procedures were performed by CCEH.

Statistical Modeling. Mean tumor volume trajectories across time were compared between groups using a parametric model. Visual inspection of growth curves suggested a quadratic model based on slight curvilinearity. Specific time points were defined from inoculation as well as from first appearance of tumor. The formal model can be expressed as $y_{ij} = \beta_0 + \beta_1 \times Group + \beta_2 \times Week + \beta_3 \times Week^2 + \beta_{12} \times Group \times Week + \beta_{13} \times Group \times Week^2 + \varepsilon_{ij}$, where y_{ij} is tumor volume for mouse i and week j, group is dummy coded for NKG2D decoy treatment group, and week is a centered time marker. Statistical hypothesis testing was conducted to assess the presence of evidence of systematic differences in model growth terms as a function of NKG2D decoy treatment group. Descriptive statistics were computed with respect to number of weeks until tumor appearance for the purposes of qualitative comparison between experimental groups.

3. Results

Structural basis of improved $NKG2D^{SCD}$ affinity. NKG2D and its ligands are glycoproteins, with six N-glycan sites per homodimer. Previous crystal structures of NKG2D alone (1MPU.pdb [46]), or in complex with MICA (1HYR.pdb [32]), ULBP3 (1KCG.pdb [47]), or ULBP6 (4S0U.pdb [48]), used protein expressed in bacterial systems, hence unmodified, leaving the question of whether

N-glycans affect its structure unanswered. To address this, DSM20, DSM25, and NKG2D[SCD] were expressed in mammalian cell-based systems that natively incorporate N-glycans. [DSM20 and DSM25 are engineered forms of MICA designed to "*pre-order*" a prominent disordered loop in the platform domain by incorporating minimal substitutions without altering ligand contacts [49].] These proteins were evaluated for crystallization alone and as complexes, yielding structures of DSM25, and NKG2D[SCD] in complexes with DSM20 and DSM25 (Table 1). Comparisons between these NKG2D[SCD] structures and previous crystal structures of native NKG2D homodimers (Figs. 1 and 2) showed that, globally, NKG2D structure did not vary considerably in response to differential ligand binding or glycosylation, with only small variations observed in overall interdomain angle and loop conformations, echoing prior analyses [40]. One to two saccharide units could be confidently modeled at expected N-glycosylation sites in the higher-resolution DSM20/NKG2D[SCD] complex structure, confirming N-glycan incorporation with minimal structural consequences. The engineered interdomain linker was fully resolvable in both NKG2D[SCD] complex structures, showing good utility of the NKG2D N-terminal arm sequence as a linking element (Supplementary Material). Our prior study [14] reported that engineering of NKG2D[SCD] yielded a concomitant orders-of-magnitude increase in affinity for MICA, though without a structure-based mechanism. The two distinct NKG2D[SCD] structures showed slightly less interdomain variation than other NKG2D structures (Fig. 1), but otherwise remarkable conservation of protomer structure across all forms and states, including key ligand-contacting side-chains (Fig. 2A, **B**, and **2C**). There was observed a subtle rotational shift in the positioning of the NKG2D[SCD] dimer on MICA ligands relative to the native homodimer (Fig. 2C) supporting the conjecture that the linked SCD construct locked the dimer in a binding-optimal conformation away from perfect dyad symmetry, effecting tighter binding.

The DSM20 and DSM25 versions of MICA are likewise highly structurally conserved with native MICA (Fig. 3A, **3B**, **3C**, and **3D**), even including the side-chains of NKG2D contacting residues. The only mutation in either variant in a contact residue occurs at position 166, with either a glutamine (MICA) or phenylalanine (DSM20). However, this substitution would not be predicted to strongly effect NKG2D binding, as the phenylalanine swaps van der Waals contacts with the side-chain of threonine 180 of NKG2D for the hydrogen bond that glutamine at this position in MICA makes with the main-chain carbonyl of isoleucine 181 of NKG2D. However, the crystal structure of free DSM25 does provide a clear explanation for the tighter binding of the DSM variants to NKG2D [49]. Free MICA has an unusual structural feature, a disordered region in the middle of the NKG2D contact surface that orders to form a helix when bound to NKG2D (Fig. 3B). It had been previously hypothesized that pre-ordering this region would increase affinity by reducing the entropic penalty to binding [49]. In the structure of free DSM25, this region achieves pre-ordering in the optimal receptor-bound conformation (Fig. 3C and **D**). The effect is likely the product of several mutations, particularly the substitution of glutamate for lysine at position 152, which adds a hydrogen bound (to the side-chain of tyrosine 157), stabilizing the helix (Fig. 4). The glutamine at position 153 in DSM20 makes the same hydrogen bond in the complex with NKG2D, so DSM20 would be predicted to have a pre-ordered helix in the unbound state, as well.
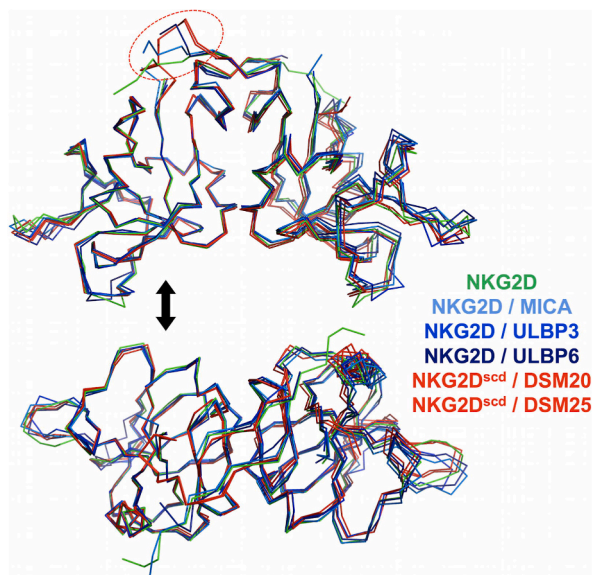

Fig. 1. NKG2D interdomain adjustments pre- and post-ligand binding. Superpositions of NKG2D α-carbon backbones, colored as indicated, showed the small range of inter-domain flexibility in the NKG2D homodimer, either in the unlinked native form, or the linked SCD form. The top and bottom views are related by an axial 90° rotation. Superpositions were performed in MacPyMOL [50,51] on the left-hand NKG2D monomer alone, indicated with the double-headed arrow, to highlight the range of flexibility. The NKG2D structure determined on its own (1MPU.pdb [46]) crystallized with a monomer in the asymmetric unit, so the dimer shown here in green represents a perfect 180° dyad relating the two monomers as a reference. The engineered connection between monomers in NKG2D[SCD] is circled with a dashed red line.
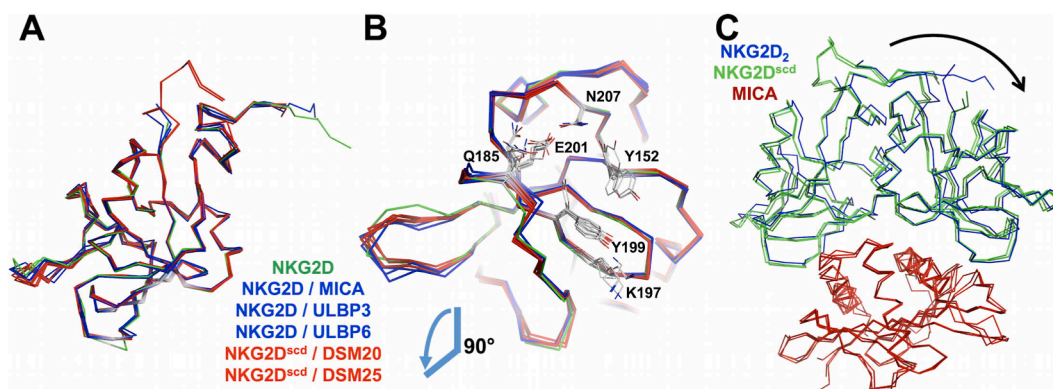
Fig. 2. Conservation of overall DSM structure. (A, B) Superpositions of NKG2D α-carbon backbones, colored as indicated, showed strong conservation of protomer structure when aligned as monomeric units. The view in B is rotated 90° from the view in A and includes the side-chains of key ligand-contacting residues. (C) The NKG2D/MICA complex (1HYR.pdb [32]) was aligned with the NKG2D/DSM20 and/DSM25 complexes (colored as indicated) on the MICA/DSM domains (red) highlighting the small rotational change in NKG2D position (arrow). Structures are shown as α-carbon backbones.
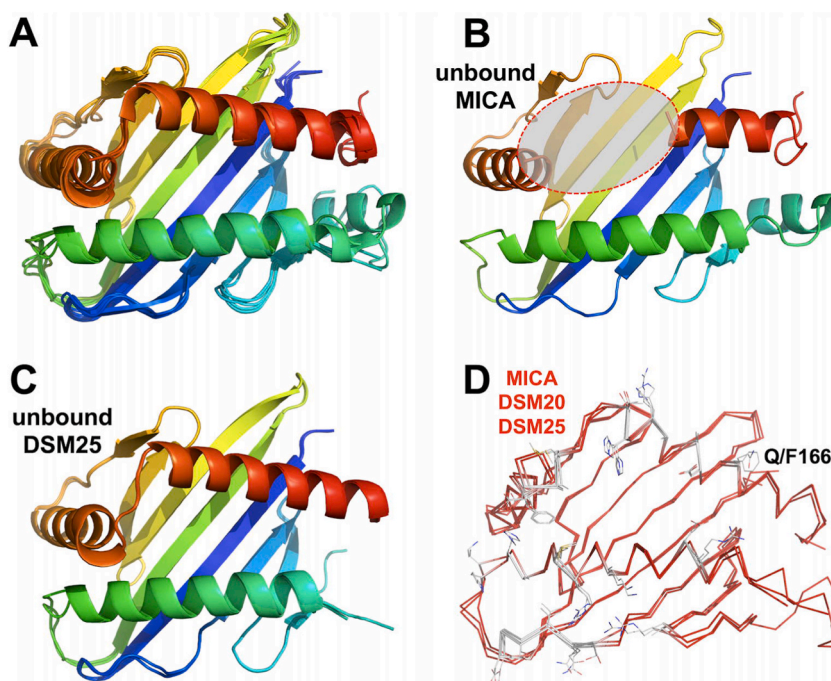
Fig. 3. Pre-organization of the MICA disordered loop. (**A**) Cartoon representations (α-helices shown as *coils*, β-strands shown as *arrows*) of the structures of MICA, DSM20, and DSM25 from all available structures were superimposed, colored from *blue* to *red* from N- to C-terminus. (**B**) The isolated structure of the MICA platform domain extracted from the structure of MICA crystallized alone (1B3J.pdb [52]), shown as in (**A**). The disordered region is highlighted with a *grey zone* edged with a *dashed red line*. (**C**) The two structures of free DSM25 in the asymmetric unit are superimposed and shown as in (**A**). (**D**) The α-carbon backbones of the structures of MICA, DSM20, and DSM25 from their respective complexes with NKG2D were superimposed. Side-chains with atoms within 4 Å of NKG2D in the complexes are shown, colored by atom type. The side-chain of the residue at position 166 is labeled.

3.1. Engineering NKG2D^{SCD}-based biologics

NKG2D poses several design challenges from the protein engineering perspective. First, monomeric NKG2D-L recognition is effected by a receptor homodimer (*e.g.*, Fig. 2C), requiring an intact dimer for functionality. Second, NKG2D is a type II transmembrane protein, flipping the usual orientation in fusion proteins. The linked NKG2D^{SCD} moiety overcomes the first challenge, rearranging fusion constructs overcomes the second, *e.g.*, in the NKG2D$_7^{SCD}$ design [14]. [The initial NKG2D$_7^{SCD}$ design incorporated seven SCD binding moieties to maximize avidity to overcome the weak affinity of native NKG2D/NKG2D-L interactions before discovering the
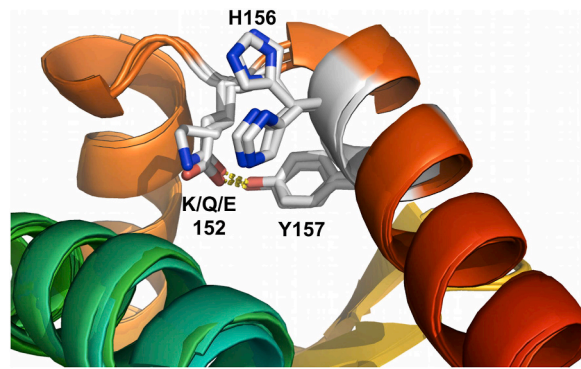
Fig. 4. MICA residues affecting pre-ordering. Cartoon representations of the structures of MICA in complex with NKG2D, and DSM20 and DSM25 in complex with NKG2Dscd, were superimposed and shown in cartoon representations. The side-chains of key residues affecting pre-ordering of the helical segment underlying the NKG2D contact surface are shown in a licorice-stick representation and labeled.

enhanced affinity inherent to the SCD design.] For these studies, NKG2D$_7^{SCD}$ was used alongside two additional designs, a bivalent design linking the SCD moiety C-terminal to an antibody Fc (NKG2D$_2^{SCD}$) and a monovalent design (NKG2D$_1^{SCD}$). [Our Fc-dimerized SCD design is distinct from previous NKG2D-Fc fusions [53–56] by virtue of the pre-assembled SCD recognition module.] All three designs incorporate cleavable, N-terminal Scn fusion partners to improve yield. These designs span a range of avidities and molecular weights to optimize solid tumor penetrance. NKG2D$_1^{SCD}$ is used without cleaving off the Scn moiety to maintain a molecular weight
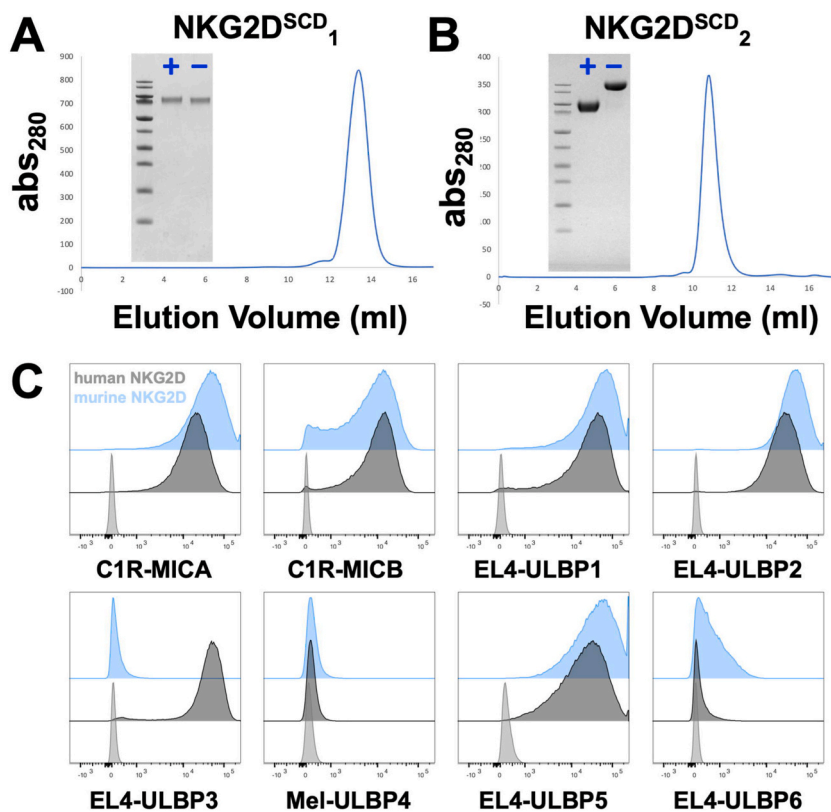

Fig. 5. Validation of NKG2D^{SCD} biologics. SEC chromatograms with inset comparative reduced (+) and non-reduced (−) PAGE analyses for (A) NKG2D$_1^{SCD}$ and (B) NKG2D$_2^{SCD}$ show solution monodispersivity, expected molecular weight, purity, and proper disulfide bond formation. (C) Flow cytometry histogram profiles show binding of PE-conjugated Fc NKG2D$_2^{SCD}$ to C1R, Mel, and EL4 cells transfected with NKG2D-L as indicated. *Blue* profiles represent NKG2D$_2^{SCD}$ incorporating murine NKG2D; *dark grey* profiles represent NKG2D$_2^{SCD}$ with human NKG2D; and *light grey* profiles represent PBS control fluorescence. NKG2D$_1^{SCD}$ was not tested by flow under the expectation that monovalent reagents would have fast enough off-rates to preclude retention and staining. Murine NKG2D$_2^{SCD}$ was tested to begin evaluating this reagent for potential use as a general NKG2D-L identification reagent, complementing human NKG2D$_2^{SCD}$.

above the glomerular filtration limit. $NKG2D_2^{SCD}$ retains interactions with Fc receptors to optimize pharmacokinetics and possibly engage antibody dependent cytotoxicity (ADCC) to enhance anti-tumor effects [53,54]. All three constructs were successfully produced as secreted proteins from transduced human cell lines, insuring proper folding and post-translational modification (Fig. 5A and **B** [14]). Functionality and specificity of the $NKG2D_2^{SCD}$ constructs with either human or murine $NKG2D^{SCD}$ domains were confirmed by flow analyses against cell lines expressing NKG2D-L (Fig. 5C [14]). $NKG2D_7^{SCD}$ was previously shown to bind all known human NKG2D-L [14], but neither human nor murine $NKG2D_2^{SCD}$ bound MEL-ULBP-4 (Fig. 5C). This behavior might be explained by a weaker NKG2D/ULBP4 affinity requiring higher valency reagents to successfully stain ULBP4+ cells. On the other hand, lack of EL4-ULBP3 staining with murine $NKG2D_2^{SCD}$ (Fig. 5C was consistent with previous reports that murine NKG2D does not bind to ULBP-3 [57]. Design schematics for each construct are shown in Fig. 6A.

3.2. $NKG2D^{SCD}$ pharmacodynamics and pharmacokinetics

Biodistribution and serum half-lives were assessed by infusing radiolabeled $NKG2D^{SCD}$ constructs into xenografted mice bearing NKG2D-L$^+$ MDAH-2774-TF flank tumors [14], tracking tissue distribution (Fig. 6A and **B**), or wild-type Balb/c mice, following clearance from circulation (Fig. 6C). Four $NKG2D^{SCD}$ constructs were used ($NKG2D_1^{SCD}$, $NKG2D_2^{SCD}$ (human or murine Fcs), and $NKG2D_7^{SCD}$); free Scn was used as a negative control. Free Scn accumulated predominantly in the renal cortex (location of the Scn receptor Megalin/LRP2 [58]) but also in the salivary gland, where all radiolabeled proteins and peptides routinely show accumulation [43,44], and intestinal tract, but minimal concentration in the tumor. $NKG2D_1^{SCD}$ showed strong tumor and liver accumulation but less relative kidney uptake, consistent with successful exclusion from the nephron. [Liver uptake can be explained by amino acid metabolism after reagent breakdown [59].] $NKG2D_2^{SCD}$ showed strong tumor, liver, and skin accumulation, the latter possibly due to cross-reactivity of murine Fc receptors for human antibodies [60]. $NKG2D_7^{SCD}$ predominately accumulated in the liver but also showed tumor uptake. $NKG2D_1^{SCD}$ showed the most even distribution throughout the tumor, consistent with improved penetrance due to its monovalency and reduced molecular weight. Serum retention was best for $NKG2D_2^{SCD}$ (human Fc), followed by $NKG2D_2^{SCD}$ (murine Fc) and $NKG2D_1^{SCD}$, and worst for $NKG2D_7^{SCD}$. Based on tumor accumulation and serum retention, $NKG2D_1^{SCD}$ $NKG2D_2^{SCD}$ (human Fc) were advanced to efficacy trials.
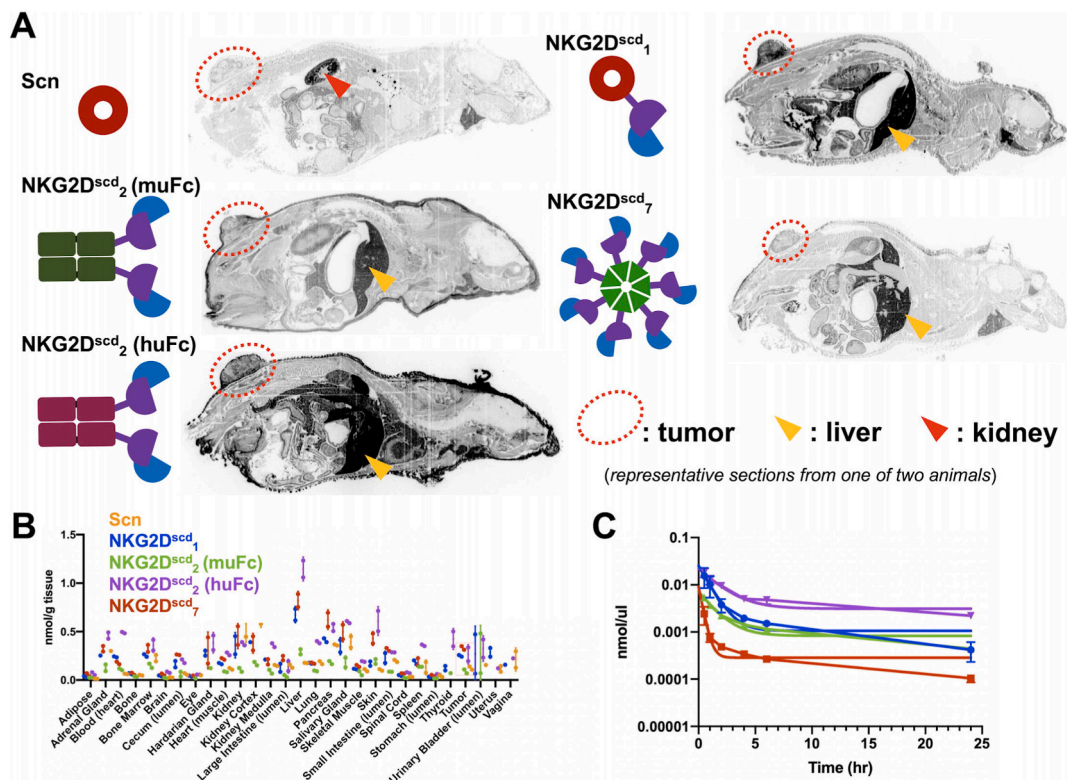

Fig. 6. $NKG2D^{SCD}$ biologic pharmacodynamics and pharmacokinetics. (A) Autoradiograms of representative sagittal sections of tumor-bearing mice show tissue distributions for ^{14}C-labeled $NKG2D^{SCD}$ biologics and Scn control. Each section is accompanied with a schematic representation of the biologic reagent, with the $NKG2D^{SCD}$ moieties colored *blue/purple* and the Scn fusion partner colored *dark red*. Flank tumors, liver, and kidney are labeled as indicated. (B) Quantitation of tissue-by-tissue label accumulation, colored by reagent as indicated. Tumor is highlighted with a *red box*. (C) Reagent clearance from the bloodstream, colored by reagent as indicated in (B).

3.3. Testing in vivo efficacy of Fc dimeric and monomeric NKG2D^{SCD}

In vivo efficacy of NKG2D$_2^{SCD}$ and NKG2D$_1^{SCD}$ was assayed using our previously established xenotransplant mouse model of NKG2D-driven tumor initiation [14]. In this model, limiting dilution subcutaneous implants of the NKG2D-L$^+$ human ovarian cancer cell line MDAH-2774 stably transfected with signaling-competent NKG2D/DAP10 (MDAH-2774-TF) displayed increased tumor take and reduced latency compared to implants using non-transfected cells in NOD SCID mice. Local application at the implant site of the prototype NKG2D$_7^{SCD}$ prevented the enhanced tumorigenicity of the MDAH-2774-TF cells and provided proof of involvement of NKG2D/NKG2D-L signaling in the generation of that phenotype [14].

In this study, NSG rather than NOD SCID mice were used requiring a re-titration experiment to determine the number of transplanted cells necessary for saturating tumor take within a few weeks post-transplant in the control group. Guided by the outcome of that experiment, groups of 10 each NSG mice were subcutaneously injected with 1×10^3 MDAH-2774-TF cells and either mock-treated or treated with one of the NKG2D^{SCD} reagents, each at three dosages, via tail vein injections up to three weeks post-transplant, schematized in Fig. 7A. Tumor development was monitored for several weeks to determine if either of the NKG2D^{SCD} reagents affected tumor take and/or latency compared to the control, and relative strengths and coarse dose responses of any observed therapeutic effects (Fig. 7b). By week two post-implantation, all the mock-treated control mice displayed palpable nodules, whereas tumor development was clearly delayed (*increased latency*) in all but the NKG2D$_2^{SCD}$ 250 µg treatment group. Treatment effects appeared qualitatively more pronounced in mice treated with the NKG2D$_1^{SCD}$ compared to the bivalent reagent. Statistically, when compared with the control group, the mean number of weeks until tumor development was 1.2 greater, 1.2 greater, and 1.0 greater in the 500 mg, 250 mg, and 50 mg NKG2D$_1^{SCD}$ treatment groups, respectively (Table 1). With NKG2D$_2^{SCD}$ treatments, the mean values were 1.1 greater, 0.4 greater, and 1.1 greater than control with 500 mg, 250 mg, and 50 mg NKG2D decoy, respectively (**Supplementary Table**). There was no treatment impact on overall tumor take, with all mice developing tumors at experimental endpoints.

We also tested if NKG2D^{SCD} reagents affected tumor growth. Treatment with NKG2D$_2^{SCD}$ at 50 µg resulted in significantly smaller tumor volumes compared to control ($p \approx 0.003$), as did treatment with the monovalent reagent at 250 µg ($p \approx 0.016$) (Fig. 8A and **B**). All other treatment conditions, when compared to the negative control group in isolation, also resulted in somewhat reduced tumor volumes but without statistical significance (Fig. 8A and **B**). There was no evidence of a dose response. When tumor volumes were controlled for the time of appearance of palpable nodules (Fig. 8C and **D**) those differences essentially disappeared or, as in the case of the NKG2D$_1^{SCD}$ 250 µg treatment group, were unexpectedly contrarian, with an apparent increase of tumor growth compared to control
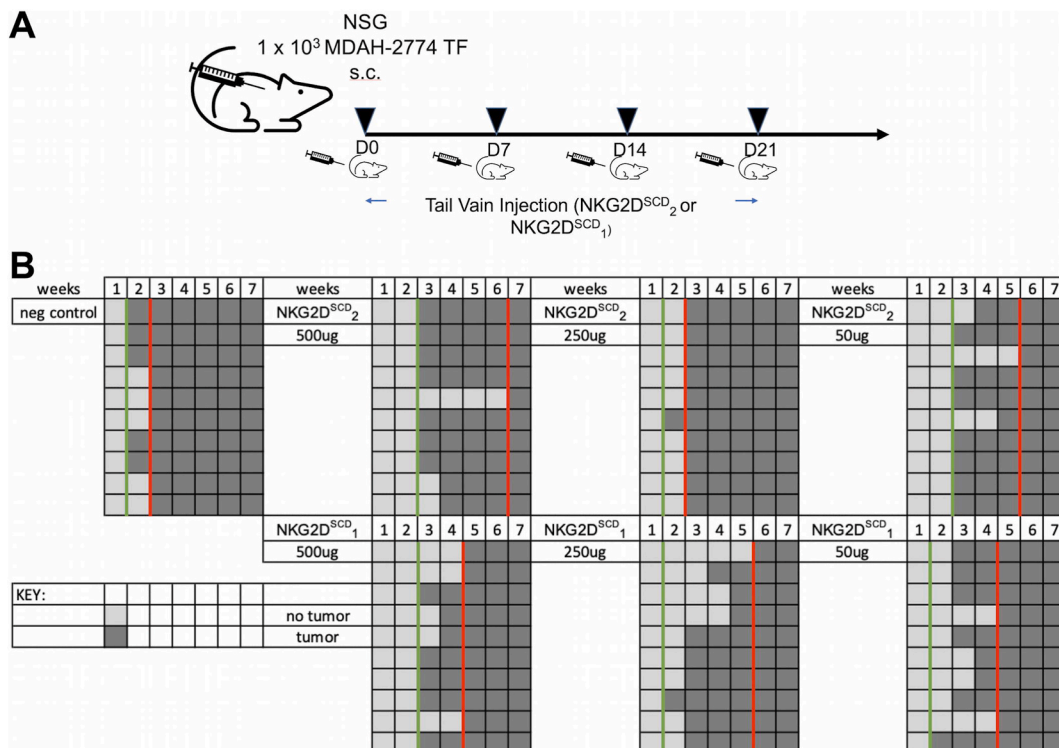

Fig. 7. Treatment with NKG2D receptor decoys delays NKG2D-driven tumor initiation. (A) A schematic shows the treatment regimen. (B) Square graph displays tumor initiation by NKG2D-L$^+$ and NKG2D+MDAH-2774-TF cells implanted subcutaneously into flanks of NSG mice in the presence or absence of NKG2D$_2^{SCD}$ or monovalent NKG2D^{SCD} at the concentrations indicated. *Dark* and *light grey* boxes indicate presence or absence of palpable tumors, respectively. Numbers indicate weeks post inoculation. *Green lines* indicate the last timepoint when no tumors are observed in any mice within a treatment group; *red lines* indicate the first timepoint when tumors are observed in all mice within a group.
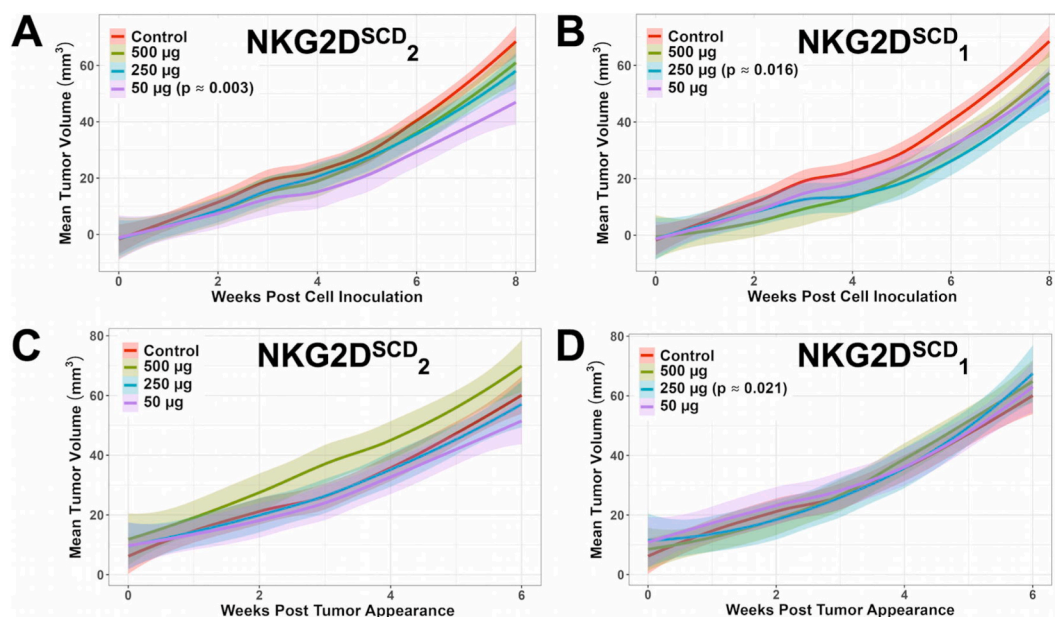
Fig. 8. NKG2D receptor decoy treatment effect on NKG2D-driven tumor growth. (A and B) Graphic representations of MDAH-2774-TF tumor volume averages from mice treated with the indicated doses of (A) NKG2D$_2^{SCD}$ or (B) NKG2D$_1^{SCD}$ or solvent control (A and B) at the indicated weekly time intervals post tumor cell inoculation. Data were derived from 10 mice each per group. (C and D) Graphic representation MDAH-2774-TF tumor volume averages normalized to times of tumor appearance. Data were derived from the same mice as in A and B. p-values highlight treatment conditions reaching significance upon comparison to Control. Global p-values for all treatment combinations among tumors measured post cell inoculation and post tumor appearance were 0.25 and 0.2, respectively.

($p \approx 0.021$).

4. Discussion

Building on our previous studies, we describe the design rationale, production, *in vitro* validation, and *in vivo* preclinical testing of three NKG2D-based, pan-NKG2D-L masking reagents: NKG2D$_7^{SCD}$, NKG2D$_2^{SCD}$, and NKG2D$_1^{SCD}$. A key feature of these designs is the incorporation of NKG2D^{SCD} recognition elements that have increased NKG2D-L affinities, for which we determined a structure-based mechanism. The motivation to develop these inhibitors of NKG2D/NKG2D-L interactions stemmed from our discovery of a counter-intuitive, tumor-promoting role for NKG2D axis signaling in advanced cancers. Therefore, antagonizing NKG2D signals in this specific context would, contrary to expectation, be predicted to have therapeutic benefits. Our designs achieve this effect with maximum coverage of NKG2D-L and minimal off-target effects and non-human sequences. [NKG2D$_2^{SCD}$ reagents, with combinations of human or murine NKG2D^{SCD} or Fc moieties, are also ideal anti-pan-NKG2D-L reagents for research applications, FYI.] This approach may also have application to autoinflammatory conditions, such as Crohn's disease, celiac sprue, inflammatory bowel disease, and rheumatoid arthritis, and organ transplantation (with reagents lacking functional Fc domains to prohibit unwanted ADCC).

We used our previously established xenotransplant model [14,61], in which signaling by NKG2D ectopically expressed by the NKG2D-L+ human ovarian cancer cell line MDAH-2774 enhances tumor initiation and promotes growth in early stages of tumor development. In this model, masking of NKG2D-L and ensuing prevention of NKG2D signaling should delay tumor take and attenuate tumor growth. Based on *in vivo* pharmacokinetic and pharmacodynamic studies, NKG2D$_1^{SCD}$ and NKG2D$_2^{SCD}$ were selected for efficacy testing. Treatment with both NKG2D$_1^{SCD}$ and NKG2D$_2^{SCD}$ resulted in increased latency and suppressed growth curves over a monitoring period of eight weeks. However, when tumor size was adjusted for appearance of palpable tumors, those effects on growth were not significant. This result is consistent with our previous observation [61] and may be explained by progressive loss of NKG2D-L on growing MDAH-2774-TF tumors. Indeed, expression of ULBP-3, the predominant NKG2D-L expressed by MDAH-2774-TF cells, was essentially absent by immunohistochemistry in all the randomly selected sentinel tumors, harvested at experimental endpoints (Fig. 9A, **9B**, **9C**, **9D**, **9E**, **9F**, **9G**, and **9H**). In addition, the absence of an apparent treatment impact on established tumor growth may be due to a timing disconnect between decoy treatment and appearance of tumor nodules. Overall NKG2D^{SCD} decoy effects did not clearly segregate with either construct type or dosage.

Progressing tumors also proteolytically shed soluble NKG2D-L (sNKG2D-L), which leads to loss of cell-surface NKG2D on lymphocytes, and functional impairment of the axis, through internalization/degradation. The degree that MDAH-2774-TF cells produce sNKG2D-L, *in vitro* or *in vivo*, was not studied, but sNKG2D-L may also complicate our analyses. Alternatively, NKG2D^{SCD} decoys may also be used to neutralize sNKG2D-L, allowing for lymphocyte NKG2D recovery in multiple disease contexts.

Finetuning of the model, treatment schedule, and dosages may yield more definitive results. Use of NSG mice also made it
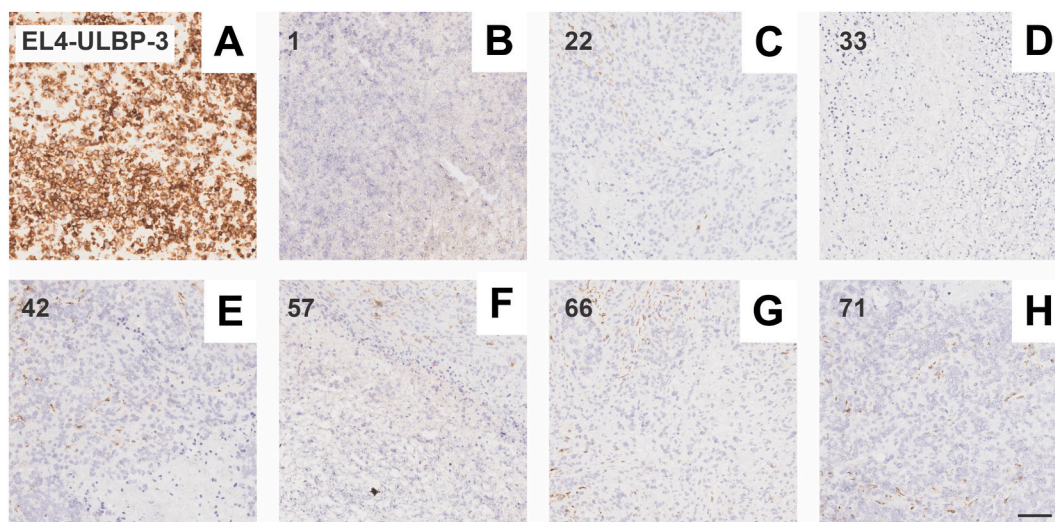
Fig. 9. MDAH-2774-TF tumors loose ULBP-3 expression. Immunohistochemistry of ULBP-3 expression in each one of three sentinel tumors per experimental group harvested at experimental endpoints shows lack of staining by most tumor cells. Upper left image shows positive control staining of EL4-ULBP3 cells (A). Numbers in the rest of the images represent mouse identifiers, from the control group (B), the NKG2D$_2^{SCD}$ 500 μg group (C), the NKG2D$_2^{SCD}$ 250 μg group (D), the NKG2D$_2^{SCD}$ 50 μg group (E), the NKG2D$_1^{SCD}$ 500 μg group (F), the NKG2D$_1^{SCD}$ 250 μg group (G), and the NKG2D$_1^{SCD}$ 50 μg group (H). Scale bar represents 100 μm.

impossible to evaluate enhanced ADCC effects of NKG2D$_2^{SCD}$ reagents. However, our goal was not to "*cure*" mice, but rather to seek evidence that NKG2D^{SCD} decoys have biologically relevant effects in an NKG2D-driven tumor model. As with many current biologics, if moved into the clinic, NKG2D decoys would likely be employed to complement a multi-modal, standard-of-care treatment regimen, in cancer as well as in other disease applications, as the theoretical effect of NKG2D axis blockade would not be expected to lead to curative outcomes in isolation.

Animal Studies

All vertebrate animal experiments were approved under FHCC Animal Care and Use Committee protocols 50808 and 51040.

Funding

Data availability statement

Crystallographic structure factors and model coordinates have been deposited in the Protein Data Bank under accession codes 8TLZ, 8TM0, and 8TM2.

CRediT authorship contribution statement

Peter B. Rupert: Writing – review & editing, Writing – original draft, Visualization, Validation, Methodology, Investigation, Formal analysis. **Matthew Buerger:** Writing – review & editing, Methodology, Investigation. **Emily J. Girard:** Writing – review & editing, Writing – original draft, Methodology, Investigation, Formal analysis, Conceptualization. **Marie Frutoso:** Writing – review & editing, Writing – original draft, Methodology, Investigation, Formal analysis. **Don Parrilla:** Writing – review & editing, Methodology, Investigation, Formal analysis. **Kevin Ng:** Writing – review & editing, Methodology, Investigation. **Theodore Gooley:** Writing – review & editing, Writing – original draft, Formal analysis. **Veronika Groh:** Writing – review & editing, Writing – original draft, Methodology, Investigation, Formal analysis, Conceptualization. **Roland K. Strong:** Writing – review & editing, Writing – original draft, Methodology, Investigation, Funding acquisition, Formal analysis, Conceptualization.

Declaration of competing interest

Appendix A. Supplementary data

Supplementary data to this article can be found online at https://doi.org/10.1016/j.heliyon.2024.e28583.

References

[1] L.L. Lanier, NKG2D receptor and its ligands in host defense, Cancer Immunol. Res. 3 (6) (2015) 575–582.
[2] S. Bauer, V. Groh, J. Wu, A. Steinle, J.H. Phillips, L.L. Lanier, et al., Activation of NK cells and T cells by NKG2D, a receptor for stress-inducible MICA, Science 285 (5428) (1999) 727–729.
[3] V. Groh, A. Bruhl, H. El-Gabalawy, J.L. Nelson, T. Spies, Stimulation of T cell autoreactivity by anomalous expression of NKG2D and its MIC ligands in rheumatoid arthritis, Proc. Natl. Acad. Sci. U.S.A. 100 (16) (2003) 9452–9457.
[4] A. Gomez-Cadena, L. Spehner, M. Kroemer, M.B. Khelil, K. Bouiller, G. Verdeil, et al., Severe COVID-19 patients exhibit an ILC2 NKG2D(+) population in their impaired ILC compartment, Cell. Mol. Immunol. 18 (2) (2021) 484–486.
[5] B. Meresse, Z. Chen, C. Ciszewski, M. Tretiakova, G. Bhagat, T.N. Krausz, et al., Coordinated induction by IL15 of a TCR-independent NKG2D signaling pathway converts CTL into lymphokine-activated killer cells in celiac disease, Immunity 21 (3) (2004) 357–366.
[6] J. Wu, Y. Song, A.B. Bakker, S. Bauer, T. Spies, L.L. Lanier, et al., An activating immunoreceptor complex formed by NKG2D and DAP10, Science 285 (5428) (1999) 730–732.
[7] D. Garrity, M.E. Call, J. Feng, K.W. Wucherpfennig, The activating NKG2D receptor assembles in the membrane with two signaling dimers into a hexameric structure, Proc. Natl. Acad. Sci. U. S. A. 102 (21) (2005) 7641–7646.
[8] J.L. Upshaw, P.J. Leibson, NKG2D-mediated activation of cytotoxic lymphocytes: unique signaling pathways and distinct functional outcomes, Semin. Immunol. 18 (3) (2006) 167–175.
[9] R.A. Eagle, J. Trowsdale, Promiscuity and the single receptor: NKG2D, Nat. Rev. Immunol. 7 (9) (2007) 737–744.
[10] S. Gonzalez, A. Lopez-Soto, B. Suarez-Alvarez, A. Lopez-Vazquez, C. Lopez-Larrea, NKG2D ligands: key targets of the immune response, Trends Immunol. 29 (8) (2008) 397–403.
[11] D.H. Raulet, S. Gasser, B.G. Gowen, W. Deng, H. Jung, Regulation of ligands for the NKG2D activating receptor, Annu. Rev. Immunol. 31 (2013) 413–441.
[12] M. Babic, C. Romagnani, The role of natural killer group 2, member D in chronic inflammation and autoimmunity, Front. Immunol. 9 (2018) 1219.
[13] A.C. Benitez, Z. Dai, H.H. Mann, R.S. Reeves, D.H. Margineantu, T.A. Gooley, et al., Expression, signaling proficiency, and stimulatory function of the NKG2D lymphocyte receptor in human cancer cells, Proc. Natl. Acad. Sci. U. S. A. 108 (10) (2011) 4081–4086.
[14] X. Cai, A. Caballero-Benitez, M.M. Gewe, I.C. Jenkins, C.W. Drescher, R.K. Strong, et al., Control of tumor initiation by NKG2D naturally expressed on ovarian cancer cells, Neoplasia 19 (6) (2017) 471–482.
[15] S. Sheppard, A. Ferry, J. Guedes, N. Guerra, The paradoxical role of NKG2D in cancer immunity, Front. Immunol. 9 (2018) 1808.
[16] M. Risti, M.D. Bicalho, MICA and NKG2D: is there an impact on kidney transplant outcome? Front. Immunol. 8 (2017) 179.
[17] M. Allez, V. Tieng, A. Nakazawa, X. Treton, V. Pacault, N. Dulphy, et al., CD4+NKG2D+ T cells in Crohn's disease mediate inflammatory and cytotoxic responses through MICA interactions, Gastroenterology 132 (7) (2007) 2346–2358.
[18] L. Petukhova, M. Duvic, M. Hordinsky, D. Norris, V. Price, Y. Shimomura, et al., Genome-wide association study in alopecia areata implicates both innate and adaptive immunity, Nature 466 (7302) (2010) 113–117.
[19] M. Allez, B.E. Skolnick, M. Wisniewska-Jarosinska, R. Petryka, R.V. Overgaard, Anti-NKG2D monoclonal antibody (NNC0142-0002) in active Crohn's disease: a randomised controlled trial, Gut 66 (11) (2017) 1918–1925.
[20] E. Breman, B. Demoulin, S. Agaugue, S. Mauen, A. Michaux, L. Springuel, et al., Overcoming target driven fratricide for T cell therapy, Front. Immunol. 9 (2018) 2940.
[21] K.A. Whalen, K. Rakhra, N.K. Mehta, A. Steinle, J.S. Michaelson, P.A. Baeuerle, Engaging natural killer cells for cancer therapy via NKG2D, CD16A and other receptors, mAbs 15 (1) (2023) 2208697.
[22] X. Cai, Z. Dai, R.S. Reeves, A. Caballero-Benitez, K.L. Duran, J.J. Delrow, et al., Autonomous stimulation of cancer cell plasticity by the human NKG2D lymphocyte receptor coexpressed with its ligands on cancer cells, PLoS One 9 (10) (2014) e108942.
[23] V. Groh, K. Smythe, Z. Dai, T. Spies, Fas-ligand-mediated paracrine T cell regulation by the receptor NKG2D in tumor immunity, Nat. Immunol. 7 (7) (2006) 755–762.
[24] F. Cesaratto, O.R. Burrone, G. Petris, Tobacco Etch Virus protease: a shortcut across biotechnologies, J. Biotechnol. 231 (2016) 239–249.
[25] V.T. Chang, M. Crispin, A.R. Aricescu, D.J. Harvey, J.E. Nettleship, J.A. Fennelly, et al., Glycoprotein structural genomics: solving the glycosylation problem, Structure 15 (3) (2007) 267–273.
[26] A.D. Bandaranayake, C. Correnti, B.Y. Ryu, M. Brault, R.K. Strong, D.J. Rawlings, Daedalus: a robust, turnkey platform for rapid production of decigram quantities of active recombinant proteins in human cell lines using novel lentiviral vectors, Nucleic Acids Res. 39 (2011) e143.
[27] Z. Otwinowski, W. Minor, Processing of X-ray diffraction data collected in oscillation mode, in: Jr. CWC, R.M. Sweet (Eds.), Meth Enzymol. 276, Academic Press, NY, 1997, pp. 307–326.
[28] A. Vagin, A. Teplyakov, Molecular replacement with MOLREP, Acta Crystallogr D Biol Crystallogr 66 (Pt 1) (2010) 22–25.
[29] M.D. Winn, C.C. Ballard, K.D. Cowtan, E.J. Dodson, P. Emsley, P.R. Evans, et al., Overview of the CCP4 suite and current developments, Acta Crystallogr D Biol Crystallogr 67 (Pt 4) (2011) 235–242.
[30] E. Potterton, P. Briggs, M. Turkenburg, E. Dodson, A graphical user interface to the CCP4 program suite, Acta Crystallogr D Biol Crystallogr 59 (Pt 7) (2003) 1131–1137.
[31] Collaborative Computational Project N, The CCP4 suite: programs for protein crystallography, Acta Crystallogr. D50 (1994) 760–763.

[32] P. Li, D.L. Morris, B.E. Willcox, A. Steinle, T. Spies, R.K. Strong, Complex structure of the activating immunoreceptor NKG2D and its MHC class I-like ligand MICA, Nat. Immunol. 2 (2001) 443–451.

[33] A.J. McCoy, R.W. Grosse-Kunstleve, P.D. Adams, M.D. Winn, L.C. Storoni, R.J. Read, Phaser crystallographic software, J. Appl. Crystallogr. 40 (2007) 658–674.

[34] G.N. Murshudov, A.A. Vagin, E.J. Dodson, Refinement of macromolecular structures by the maximum-likelihood method, Acta Crystallogr D Biol Crystallogr 53 (Pt 3) (1997) 240–255.

[35] P. Emsley, K. Cowtan, Coot: model-building tools for molecular graphics, Acta Crystallogr D Biol Crystallogr 60 (Pt 12 Pt 1) (2004) 2126–2132.

[36] M.D. Winn, M.N. Isupov, G.N. Murshudov, Use of TLS parameters to model anisotropic displacements in macromolecular refinement, Acta Crystallogr. D57 (Pt 1) (2001) 122–133.

[37] R.A. Laskowski, M.W. MacArthur, D.S. Moss, J.M. Thornton, PROCHECK: a program to check the stereochemical quality of protein structures, J. Appl. Crystallogr. 26 (1993) 283–291.

[38] I.W. Davis, A. Leaver-Fay, V.B. Chen, J.N. Block, G.J. Kapral, X. Wang, et al., MolProbity: all-atom contacts and structure validation for proteins and nucleic acids, Nucleic Acids Res. 35 (Web Server issue) (2007) W375–W383.

[39] H.M. Berman, J. Westbrook, Z. Feng, G. Gilliland, T.N. Bhat, H. Weissig, et al., The protein Data Bank, Nucleic Acids Res. 28 (1) (2000) 235–242.

[40] B.J. McFarland, R.K. Strong, Thermodynamic analysis of degenerate recognition by the NKG2D immunoreceptor: not induced fit but rigid adaptation, Immunity 19 (6) (2003) 803–812.

[41] N. Jentoft, D.G. Dearborn, Protein labeling by reductive alkylation, Methods Enzymol. 91 (1983) 570–579.

[42] N. Jentoft, D.G. Dearborn, Labeling of proteins by reductive methylation using sodium cyanoborohydride, J. Biol. Chem. 254 (11) (1979) 4359–4365.

[43] Sangar ML. Cook, E.J. Girard, G. Hopping, C. Yin, F. Pakiam, M.Y. Brusniak, et al., A potent peptide-steroid conjugate accumulates in cartilage and reverses arthritis without evidence of systemic corticosteroid exposure, Sci. Transl. Med. 12 (533) (2020).

[44] Z.R. Crook, E. Girard, G.P. Sevilla, M. Merrill, D. Friend, P.B. Rupert, et al., A TfR-binding cystine-dense peptide promotes blood-brain barrier penetration of bioactive molecules, J. Mol. Biol. 432 (14) (2020) 3989–4009.

[45] Y. Zhang, M. Huo, J. Zhou, S. Xie, PKSolver: an add-in program for pharmacokinetic and pharmacodynamic data analysis in Microsoft Excel, Comput. Methods Progr. Biomed. 99 (3) (2010) 306–314.

[46] B.J. McFarland, T. Kortemme, S.F. Yu, D. Baker, R.K. Strong, Symmetry recognizing asymmetry. Analysis of the interactions between the C-type lectin-like immunoreceptor NKG2D and MHC class I-like ligands, Structure (Camb) 11 (4) (2003) 411–422.

[47] S. Radaev, B. Rostro, A.G. Brooks, M. Colonna, P.D. Sun, Conformational plasticity revealed by the cocrystal structure of NKG2D and its class I MHC-like ligand ULBP3, Immunity 15 (6) (2001) 1039–1049.

[48] J. Zuo, C.R. Willcox, F. Mohammed, M. Davey, S. Hunter, K. Khan, et al., A disease-linked ULBP6 polymorphism inhibits NKG2D-mediated target cell killing by enhancing the stability of NKG2D ligand binding, Sci. Signal. 10 (481) (2017).

[49] C.S. Lengyel, L.J. Willis, P. Mann, D. Baker, T. Kortemme, R.K. Strong, et al., Mutations designed to destabilize the receptor-bound conformation increase MICA-NKG2D association rate and affinity, J. Biol. Chem. 282 (42) (2007) 30658–30666.

[50] L.L.C. Schrodinger, The PyMOL Molecular Graphics System, 2010, Version 1.3r1.

[51] W.L. DeLano, The PyMOL Molecular Graphics System, DeLano Scientific, San Carlos, CA, USA, 2002.

[52] P. Li, S.T. Willie, S. Bauer, D.L. Morris, T. Spies, R.K. Strong, Crystal structure of the MHC class I homolog MIC-A, a gammadelta T cell ligand, Immunity 10 (5) (1999) 577–584.

[53] J. Steinbacher, K. Baltz-Ghahremanpour, B.J. Schmiedel, A. Steinle, G. Jung, A. Kubler, et al., An Fc-optimized NKG2D-immunoglobulin G fusion protein for induction of natural killer cell reactivity against leukemia, Int. J. Cancer 136 (5) (2015) 1073–1084.

[54] S. Raab, J. Steinbacher, B.J. Schmiedel, P.C. Kousis, A. Steinle, G. Jung, et al., Fc-optimized NKG2D-Fc constructs induce NK cell antibody-dependent cellular cytotoxicity against breast cancer cells independently of HER2/neu expression status, J. Immunol. 193 (8) (2014) 4261–4272.

[55] P.H. Feng, P. Lam, S.H. Tseng, Y.J. Kung, E. Farmer, M.A. Cheng, et al., NKG2D-Fc fusion protein promotes antitumor immunity through the depletion of immunosuppressive cells, Cancer Immunol. Immunother. 69 (10) (2020) 2147–2155.

[56] B. Zhang, S. Kracker, T. Yasuda, S. Casola, M. Vanneman, C. Homig-Holzel, et al., Immune surveillance and therapy of lymphomas driven by Epstein-Barr virus protein LMP1 in a mouse model, Cell 148 (4) (2012) 739–751.

[57] H.G. Wirsching, H. Zhang, F. Szulzewsky, S. Arora, P. Grandi, P.J. Cimino, et al., Arming oHSV with ULBP3 drives abscopal immunity in lymphocyte-depleted glioblastoma, JCI Insight 4 (13) (2019).

[58] S.A. Jaberi, A. Cohen, C. D'Souza, Y.M. Abdulrazzaq, S. Ojha, S. Bastaki, et al., Lipocalin-2: structure, function, distribution and role in metabolic disorders, Biomed. Pharmacother. 142 (2021) 112002.

[59] Y. Hou, S. Hu, X. Li, W. He, G. Wu, Amino acid metabolism in the liver: nutritional and physiological significance, Adv. Exp. Med. Biol. 1265 (2020) 21–37.

[60] G. Dekkers, A.E.H. Bentlage, T.C. Stegmann, H.L. Howie, S. Lissenberg-Thunnissen, J. Zimring, et al., Affinity of human IgG subclasses to mouse Fc gamma receptors, mAbs 9 (5) (2017) 767–773.

[61] A. El-Gazzar, X. Cai, R.S. Reeves, Z. Dai, A. Caballero-Benitez, D.L. McDonald, et al., Effects on tumor development and metastatic dissemination by the NKG2D lymphocyte receptor expressed on cancer cells, Oncogene 33 (41) (2014) 4932–4940.